Measurement of ν_μ charged-current inclusive π^0 production in the NOvA near detector

M. A. Acero,[2] P. Adamson,[12] G. Agam,[21] L. Aliaga,[12] T. Alion,[40] V. Allakhverdian,[27] S. Altakarli,[47] N. Anfimov,[27] A. Antoshkin,[27] L. Asquith,[40] E. Arrieta-Diaz,[31] A. Aurisano,[6] A. Back,[24] M. Baird,[19,40,46] N. Balashov,[27] P. Baldi,[25] B. A. Bambah,[17] S. Bashar,[44] K. Bays,[4,21] S. Bending,[45] R. Bernstein,[12] V. Bhatnagar,[33] B. Bhuyan,[14] J. Bian,[25,32] J. Blair,[16] A. C. Booth,[40] P. Bour,[9] C. Bromberg,[29] N. Buchanan,[8] A. Butkevich,[22] S. Calvez,[8] M. Campbell,[45] T. J. Carroll,[43,49] E. Catano-Mur,[24,48] S. Childress,[12] B. C. Choudhary,[11] B. Chowdhury,[36] T. E. Coan,[38] M. Colo,[48] L. Corwin,[37] L. Cremonesi,[45] G. S. Davies,[19] P. F. Derwent,[12] R. Dharmapalan,[1] P. Ding,[12] Z. Djurcic,[1] M. Dolce,[44] D. Doyle,[8] E. C. Dukes,[46] D. Dueñas Tonguino,[6] P. Dung,[43] H. Duyang,[36] S. Edayath,[7] R. Ehrlich,[46] G. J. Feldman,[15] P. Filip,[23] W. Flanagan,[10] M. J. Frank,[35,46] H. R. Gallagher,[44] R. Gandrajula,[29] F. Gao,[34] S. Germani,[45] A. Giri,[18] R. A. Gomes,[13] M. C. Goodman,[1] V. Grichine,[28] M. Groh,[19] R. Group,[46] B. Guo,[36] A. Habig,[30] F. Hakl,[20] A. Hall,[46] J. Hartnell,[40] R. Hatcher,[12] A. Hatzikoutelis,[42] K. Heller,[32] V. Hewes,[6] A. Himmel,[12] A. Holin,[45] B. Howard,[19] J. Huang,[43] J. Hylen,[12] F. Jediny,[9] C. Johnson,[8] M. Judah,[8] I. Kakorin,[27] D. Kalra,[33] D. M. Kaplan,[21] R. Keloth,[7] O. Klimov,[27] L. W. Koerner,[16] L. Kolupaeva,[27] S. Kotelnikov,[28] A. Kreymer,[12] M. Kubu,[9] Ch. Kullenberg,[27] A. Kumar,[33] C. D. Kuruppu,[36] V. Kus,[9] T. Lackey,[19] K. Lang,[43] L. Li,[25] S. Lin,[8] A. Lister,[49] M. Lokajicek,[23] S. Luchuk,[22] K. Maan,[33] S. Magill,[1] W. A. Mann,[44] M. L. Marshak,[32] M. Martinez-Casales,[24] V. Matveev,[22] B. Mayes,[40] D. P. Méndez,[40] M. D. Messier,[19] H. Meyer,[47] T. Miao,[12] W. H. Miller,[32] S. R. Mishra,[36] A. Mislivec,[32] R. Mohanta,[17] A. Moren,[30] L. Mualem,[4] M. Muether,[47] S. Mufson,[19] K. Mulder,[45] R. Murphy,[19] J. Musser,[19] D. Naples,[34] N. Nayak,[25] J. K. Nelson,[48] R. Nichol,[45] G. Nikseresht,[21] E. Niner,[12] A. Norman,[12] A. Norrick,[12] T. Nosek,[5] A. Olshevskiy,[27] T. Olson,[44] J. Paley,[12] R. B. Patterson,[4] G. Pawloski,[32] D. Pershey,[4] O. Petrova,[27] R. Petti,[36] D. D. Phan,[43] S. Phan-Budd,[50] R. K. Plunkett,[12] B. Potukuchi,[26] C. Principato,[46] F. Psihas,[19] A. Radovic,[48] A. Rafique,[1] V. Raj,[4] R. A. Rameika,[12] B. Rebel,[12,49] P. Rojas,[8] V. Ryabov,[28] O. Samoylov,[27] M. C. Sanchez,[24] S. Sánchez Falero,[24] I. S. Seong,[25] P. Shanahan,[12] A. Sheshukov,[27] P. Singh,[11] V. Singh,[3] E. Smith,[19] J. Smolik,[9] P. Snopok,[21] N. Solomey,[47] E. Song,[46] A. Sousa,[6] K. Soustruznik,[5] M. Strait,[32] L. Suter,[12] A. Sutton,[46] R. L. Talaga,[1] B. Tapia Oregui,[43] P. Tas,[5] R. B. Thayyullathil,[7] J. Thomas,[45,49] E. Tiras,[24] D. Torbunov,[32] J. Tripathi,[33] A. Tsaris,[12] Y. Torun,[21] J. Urheim,[19] P. Vahle,[48] J. Vasel,[19] P. Vokac,[9] T. Vrba,[9] M. Wallbank,[6] T. K. Warburton,[24] M. Wetstein,[24] M. While,[37] D. Whittington,[41,19] D. A. Wickremasinghe,[12] S. G. Wojcicki,[39] J. Wolcott,[44] A. Yallappa Dombara,[41] K. Yonehara,[12] S. Yu,[1,21] Y. Yu,[21] S. Zadorozhnyy,[22] J. Zalesak,[23] Y. Zhang,[40] and R. Zwaska[12]

(NOvA Collaboration)

[1]*Argonne National Laboratory, Argonne, Illinois 60439, USA*
[2]*Universidad del Atlantico, Carrera 30 No. 8-49, Puerto Colombia, Atlantico, Colombia*
[3]*Department of Physics, Institute of Science, Banaras Hindu University, Varanasi 221 005, India*
[4]*California Institute of Technology, Pasadena, California 91125, USA*
[5]*Charles University, Faculty of Mathematics and Physics, Institute of Particle and Nuclear Physics, Prague, Czech Republic*
[6]*Department of Physics, University of Cincinnati, Cincinnati, Ohio 45221, USA*
[7]*Department of Physics, Cochin University of Science and Technology, Kochi 682 022, India*
[8]*Department of Physics, Colorado State University, Fort Collins, Colorado 80523-1875, USA*
[9]*Czech Technical University in Prague, Brehova 7, 115 19 Prague 1, Czech Republic*
[10]*University of Dallas, 1845 E Northgate Drive, Irving, Texas 75062 USA*
[11]*Department of Physics and Astrophysics, University of Delhi, Delhi 110007, India*
[12]*Fermi National Accelerator Laboratory, Batavia, Illinois 60510, USA*
[13]*Instituto de Física, Universidade Federal de Goiás, Goiânia, Goiás 74690-900, Brazil*
[14]*Department of Physics, IIT Guwahati, Guwahati 781 039, India*
[15]*Department of Physics, Harvard University, Cambridge, Massachusetts 02138, USA*
[16]*Department of Physics, University of Houston, Houston, Texas 77204, USA*
[17]*School of Physics, University of Hyderabad, Hyderabad 500 046, India*
[18]*Department of Physics, IIT Hyderabad, Hyderabad 502 205, India*
[19]*Indiana University, Bloomington, Indiana 47405, USA*
[20]*Institute of Computer Science, The Czech Academy of Sciences, 182 07 Prague, Czech Republic*
[21]*Department of Physics, Illinois Institute of Technology, Chicago, Illinois 60616, USA*
[22]*Institute for Nuclear Research of Russia, Academy of Sciences 7a, 60th October Anniversary Prospect, Moscow 117312, Russia*

[23]*Institute of Physics, The Czech Academy of Sciences, 182 21 Prague, Czech Republic*
[24]*Department of Physics and Astronomy, Iowa State University, Ames, Iowa 50011, USA*
[25]*Department of Physics and Astronomy, University of California at Irvine, Irvine, California 92697, USA*
[26]*Department of Physics and Electronics, University of Jammu, Jammu Tawi,*
180 006 Jammu and Kashmir, India
[27]*Joint Institute for Nuclear Research, Dubna, Moscow region 141980, Russia*
[28]*Nuclear Physics and Astrophysics Division, Lebedev Physical Institute,*
Leninsky Prospect 53, 119991 Moscow, Russia
[29]*Department of Physics and Astronomy, Michigan State University, East Lansing, Michigan 48824, USA*
[30]*Department of Physics and Astronomy, University of Minnesota Duluth, Duluth, Minnesota 55812, USA*
[31]*Universidad del Magdalena, Carrera 32 No 22–08 Santa Marta, Colombia*
[32]*School of Physics and Astronomy, University of Minnesota Twin Cities,*
Minneapolis, Minnesota 55455, USA
[33]*Department of Physics, Panjab University, Chandigarh 160 014, India*
[34]*Department of Physics, University of Pittsburgh, Pittsburgh, Pennsylvania 15260, USA*
[35]*Department of Physics, University of South Alabama, Mobile, Alabama 36688, USA*
[36]*Department of Physics and Astronomy, University of South Carolina,*
Columbia, South Carolina 29208, USA
[37]*South Dakota School of Mines and Technology, Rapid City, South Dakota 57701, USA*
[38]*Department of Physics, Southern Methodist University, Dallas, Texas 75275, USA*
[39]*Department of Physics, Stanford University, Stanford, California 94305, USA*
[40]*Department of Physics and Astronomy, University of Sussex,*
Falmer, Brighton BN1 9QH, United Kingdom
[41]*Department of Physics, Syracuse University, Syracuse, New York 13210, USA*
[42]*Department of Physics and Astronomy, University of Tennessee, Knoxville, Tennessee 37996, USA*
[43]*Department of Physics, University of Texas at Austin, Austin, Texas 78712, USA*
[44]*Department of Physics and Astronomy, Tufts University, Medford, Massachusetts 02155, USA*
[45]*Physics and Astronomy Department, University College London,*
Gower Street, London WC1E 6BT, United Kingdom
[46]*Department of Physics, University of Virginia, Charlottesville, Virginia 22904, USA*
[47]*Department of Mathematics, Statistics, and Physics, Wichita State University,*
Wichita, Kansas 67206, USA
[48]*Department of Physics, William & Mary, Williamsburg, Virginia 23187, USA*
[49]*Department of Physics, University of Wisconsin-Madison, Madison, Wisconsin 53706, USA*
[50]*Department of Physics, Winona State University, P.O. Box 5838, Winona, Minnesota 55987, USA*

Cross sections for the interaction $\nu_\mu A \to \mu^- \pi^0 X$ with neutrino energies between 1 and 5 GeV are measured using a sample of 165,000 selected events collected in the NOvA experiment's near detector, a hydrocarbon-based detector exposed to the Neutrinos from the Main Injector beam at the Fermi National Accelerator Laboratory. Results are presented as a flux-averaged total cross section and as differential cross sections in the momenta and angles of the outgoing muon and π^0, the total four-momentum transfer, and the invariant mass of the hadronic system. Comparisons are made with predictions from a reference version of the GENIE neutrino interaction generator. The measured total cross section of $(3.57 \pm 0.44) \times 10^{-39}$ cm^2 is 7.5% higher than the GENIE prediction, but is consistent within experimental errors.

I. INTRODUCTION

Muon-neutrino-induced charged-current (CC) π^0 production on a nuclear target, hereinafter "CCπ^0," is the reaction

$$\nu_\mu A \to \mu^- \pi^0 X, \tag{1}$$

where A is the target nucleus and X represents the final-state nucleus plus any additional reaction products, possibly

including other charged or neutral pions. This channel is of particular interest for experiments studying $\nu_\mu \to \nu_e$ flavor oscillations not only because it can directly lead to backgrounds in those measurements, but also because of its close relation to the important background process of neutral current π^0 production. Events in which only one photon from the π^0 decay is reconstructed can be mistaken as containing a primary electron, the defining characteristic of a ν_e CC event.

Improved understanding of neutrino-nucleus interactions is of great benefit for the current and next generation of neutrino oscillation experiments. Experiments such as NOvA [1] and DUNE [2] lie in the few-GeV transition region between the low-energy regime dominated by quasielastic (QE) scattering and the high-energy regime dominated by deep-inelastic scattering (DIS). In addition to QE and DIS events, this transition region has a large component of baryon resonance (Res) events in which a neutrino scatters off a nucleon producing an intermediate $\Delta(1232)$ or higher-mass baryon. Pions are commonly produced in both DIS and resonant baryon interactions but through very different production mechanisms. The picture is complicated further in a nuclear medium by final-state interactions (FSIs), in which outgoing hadronic particles may strongly interact with nucleons before escaping the target nucleus. Experiments are sensitive only to particles exiting the nucleus, making it difficult to attribute observed discrepancies with a model to either the neutrino interaction or subsequent FSI effects.

The first measurements of neutrino-induced π^0 production were exclusive analyses of bubble chamber data [3,4]. Exclusive or semi-inclusive cross sections on hydrocarbon targets have been studied in MINERvA [5–7], MiniBooNE [8], and K2K [9]. Charged-current π^0 production on argon has also been recently measured in MicroBooNE [10]. The present analysis examines fully inclusive π^0 production on a primarily hydrocarbon target.

We present measurements of the $CC\pi^0$ flux-averaged total cross section as well as cross sections differential in p_π, $\cos\theta_\pi$, p_μ, $\cos\theta_\mu$, lepton momentum transfer Q^2 as defined below in Eq. (6), and the invariant mass W of the hadronic system as defined below in Eq. (8). The data used for these measurements were collected between August 2014 and January 2016 and correspond to an exposure of 3.72×10^{20} protons on target (POT) using a predominantly ν_μ beam. 165,000 events are selected as ν_μ CC candidates, of which simulation predicts 34% are signal $CC\pi^0$. A subsequent fit to a $CC\pi^0$ event classifier variable provides a final stage of background separation and signal rate estimation. With this large dataset, the uncertainty is dominated by systematic sources.

II. THE NOvA EXPERIMENT

The NOvA experiment [1] is designed to measure neutrino oscillations over an 810 km baseline. It uses two functionally identical detectors situated along the neutrinos at the main injector (NuMI) beam from the Fermi National Accelerator Laboratory (Fermilab). The NOvA near detector (ND) is located 1 km downstream of the beam target where it is subject to an intense neutrino flux. The ND has recorded millions of neutrino and antineutrino interactions, allowing large-sample neutrino cross section measurements.

A. The NuMI beam

The NuMI neutrino beam [11] is created by directing 120 GeV protons from the Fermilab main injector onto a graphite target. The many charged pions and kaons produced in the collision are focused through two magnetic horns and allowed to decay in a 650 m decay pipe to produce the primarily ν_μ neutrino beam. The NOvA detectors are located 14.6 mrad off axis relative to the beam centerline, resulting in a narrow band flux peaked at $E_\nu = 1.8$ GeV. There are two classes of impurity in the neutrino flux in the neutrino-dominated beam configuration: $\bar{\nu}_\mu$, which accounts for 1.8% of neutrinos in the 1–3 GeV region around the beam peak, and $\nu_e + \bar{\nu}_e$, which accounts for 0.7% in the same energy range.

B. The NOvA near detector

The ND is a tracking calorimeter with fine segmentation relative to the 40 cm radiation length for precise imaging of electromagnetic showers. The detector is built of polyvinyl chloride (PVC) cells with a 3.9 cm (transverse) by 6.6 cm (longitudinal) cross section and a length of 3.9 m. A detector plane consists of 96 cells, and planes are arranged in alternating vertical and horizontal orientations, allowing 3D reconstruction of observed events. The fully active volume of the detector is 12.8 m in length, consisting of 192 contiguous planes. Each detector cell is filled with a liquid scintillator blend that is 95% mineral oil and 5% pseudocumene with trace concentrations of wavelength shifting fluors [12]. Each cell contains a wavelength shifting fiber that collects and delivers light to an avalanche photodiode.

Additionally, a muon range stack is situated at the downstream end of the detector, consisting of 11 pairs of readout planes with a layer of 10.2-cm-thick steel between adjacent pairs. The range stack increases the muon energy that can be contained in the detector to about 4.5 GeV.

The interaction fiducial volume does not include any part of the range stack, limiting the relevant nuclear targets to those in the PVC and scintillator. A precise accounting of the scattering material is given in Sec. VI C.

III. EVENT SIMULATION

Predicted event rates are calculated with a detailed simulation in three stages: production and transport of

the neutrino beam, neutrino interaction, and detector response.

A. Neutrino beam simulation

Simulated outgoing hadrons from proton-nucleus collisions within the NuMI target are modeled with FLUKA [13,14]. The charged pions and kaons are subsequently propagated via FLUGG [15] through the focusing horns and into the decay pipe until their decay.

The neutrino flux prediction is improved according to the PPFX [16] framework. PPFX combines hadron-production data from an extensive survey of proton-nucleus scattering experiments and is used to constrain the predicted hadron multiplicities exiting the target. Both the central value and error band from the PPFX prediction are used. The central value for the neutrino flux integrated between 1 and 5 GeV after PPFX corrections is 8.2% lower than the raw FLUKA and FLUGG prediction.

B. Neutrino interaction simulation

Neutrino interactions are simulated with GENIE [17] v2.10.2. The GENIE simulation generates interactions via its four default production processes: quasielastic scattering, resonant baryon production, deep-inelastic scattering, and coherent pion production. Particles created via these primary processes are subsequently propagated though the nuclear medium using GENIE's hA effective cascade FSI model [18,19].

For quasielastic interactions, GENIE uses a Llewellyn Smith parameterization [20]. Resonant baryon production follows the Rein-Sehgal model [21], which calculates the resonant cross section through production and decay of $\Delta(1232)$ and higher-mass N^* baryon resonances. Coherent pion-production interactions are also simulated with the Rein-Sehgal model. Deep-inelastic scattering interactions are generated according to the Bodek-Yang model [22].

Meson exchange current (MEC) interactions are insignificant in this measurement given the signal selection, which requires evidence of a neutral pion. So that GENIE can be used in its documented default configuration and to avoid concerns over certain specifics of early MEC models in this GENIE version, MEC events were not enabled in the baseline simulation. Note that the similar quasielastic channel represents 0.4% of the selected sample. The negligible impact of MEC events on the reported cross sections was confirmed using a separate simulated event sample based on the empirical Dytman MEC model [23].

C. Detector response simulation

Final-state particles produced by GENIE are propagated through the detector using Geant 4.9.6.p04d [24]. Optical photon production is modeled with the Birks-Chou parameterization [25] for scintillator response. The light collection, signal transport in the fibers, and photodiode and

TABLE I. Definition of the signal region for CCπ^0 interactions. The left column specifies kinematic regions excluded from the signal definition, while the right lists the motivation for excluding events that lie in the excluded regions.

Kinematic exclusion	Motivation
$p_\pi > 3$ GeV/c	Negligible rate
$p_\mu > 4$ GeV/c	Long muons uncontained
$E_\nu < 1$ GeV	Background dominated
$E_\nu > 5$ GeV	Imprecise flux modeling
$Q^2 > 3$ GeV^2/c^2	Negligible rate
$W < 1$ GeV/c^2	Background dominated
$W > 3$ GeV/c^2	Negligible rate

electronics response are modeled using custom simulation software [26]. The detector is calibrated using minimum-ionizing portions of stopping cosmic ray muon tracks. The detector response to hadronic tracks and electromagnetic showers is tested using two control samples, each discussed in detail in Sec. VII E.

IV. SIGNAL DEFINITION

For this analysis, a CCπ^0 event is defined as any ν_μ CC event with at least one π^0 emerging from the struck nucleus. This definition includes events with multiple neutral or charged pions in the final state. Multi-π events are common at NOvA energies, representing 54% of CCπ^0 events in this analysis and also accounting for the majority of neutral current (NC) and ν_μ-induced CC backgrounds in the NOvA $\nu_\mu \to \nu_e$ oscillation measurement [1].

Signal events are further required to lie within the kinematic region specified in Table I. The table also gives the rationale for the kinematic exclusions applied. Selected CCπ^0 events whose true kinematics lie outside these ranges but that leak into the selected sample are treated as an analysis background and comprise only 0.2% of the sample.

V. EVENT RECONSTRUCTION AND SELECTION

An illustrative simulated $\nu_\mu A \to \mu^-\pi^0 X$ resonant event as it would appear in the ND is shown in Fig. 1. In this event, a π^0 decays promptly via $\pi^0 \to \gamma\gamma$ (branching ratio 98.8% [27]). Each decay photon produces an electromagnetic cascade. In this example event, one of the photons is on a very transverse trajectory and is visible and reconstructable only in the yz view.

A. Base reconstruction

A clustering algorithm [28] groups a collection of active detector cells ("hits") nearby in space and time into a "slice," intended to represent an individual neutrino interaction. Within each slice, an interaction vertex is reconstructed by minimizing the angular spread of hits relative to
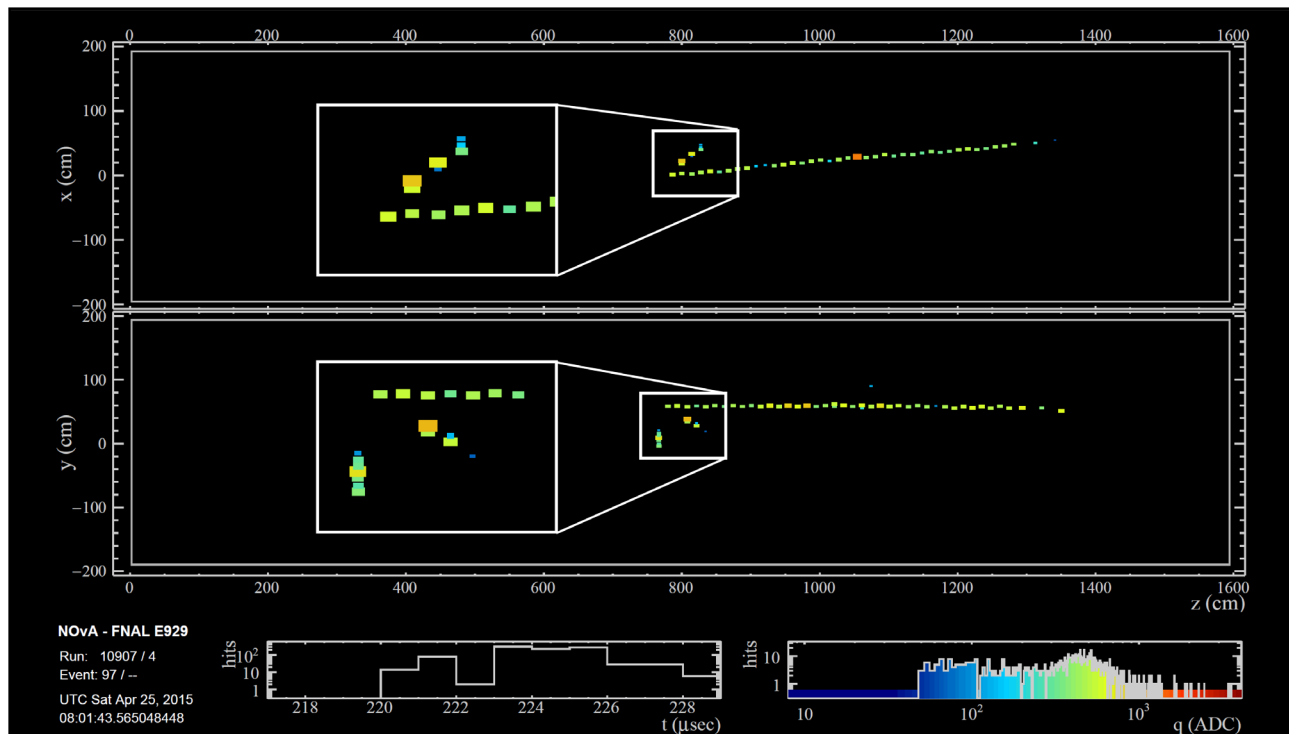
FIG. 1. An example simulated ND event. The overhead view (top) of the particle tracks in the detector and (bottom) the side view of the same tracks. In each view, a small white box shows the vertex region, with a magnified version shown in a large white box. Individual detector cells with recorded energy depositions are shown as colored rectangles, with the size and color of the rectangle related to the amplitude of the detected signal. The beam enters the detector from the left. The μ^- is seen as the long, forward-directed track. In the side view (bottom), two photons from a π^0 decay are visible. In the overhead view (top), one of the decay photons is unseen as its highly transverse trajectory stayed within a single yz detector plane.

the candidate vertex [29]. Final-state particles and electromagnetic cascades, as from photons, are reconstructed into "prongs" using a fuzzy k-means algorithm [30] that clusters hits lying along a common direction relative to the vertex. Separately, a Kalman filter algorithm [31] is applied to the event to better reconstruct muonlike tracks and to provide an energy estimate for them. A k-nearest-neighbors classifier from previous NOvA analyses [32] is used to identify the most muonlike track in each event, which is taken to be the μ^- candidate.

B. Photon identification

Candidate photon prongs are required to have a number of hits $N_{\text{hit}} \geq 10$ so that particle identification can be carried out effectively. The calorimetric energy E_{cal}, defined as the sum of the calibrated energy deposited in all of the prong's hits, must also satisfy $E_{\text{cal}} > 100$ MeV, roughly the energy deposited by a ten-hit minimum-ionizing track. For prongs satisfying these thresholds, a likelihood ratio between photon and nonphoton particle hypotheses is calculated based on the following four inputs:

(1) Bragg peak identifier: ratio of average energy deposition in the furthest six hits from the prong start point (or five hits if $10 \leq N_{\text{hit}} < 12$) to the average energy deposition in the rest of the prong.

This ratio gives a measure of the increase in dE/dx toward the end of a prong.

(2) Energy per hit: average calorimetric energy of all hits within the prong.

(3) Reconstructed gap: distance from the reconstructed event vertex to the candidate prong's start point.

(4) Missing planes along prong: largest number of consecutive planes without any energy deposition in the prong.

Figure 2 shows distributions of these four quantities for prongs in the simulated neutrino event sample. A number of familiar features can be seen. Proton prongs exhibit the most prominent Bragg peak, while the electromagnetic cascades from photons score the lowest in that variable. Protons have the highest dE/dx (thus, highest energy per hit) of the listed particles. Initial photons can lead to large prong start gaps due to the radiation length in the detector, and the subsequent cascades can skip over planes due to secondary photons.

There are significant correlations between the Bragg peak identifier and the mean energy per hit and, separately, between the reconstructed gap and missing planes along the prong. The correlations within each of these pairs are exploited when calculating the photon and nonphoton likelihoods. For numerical convenience, the logarithm of the likelihood ratio is used in calculations, equivalent to the
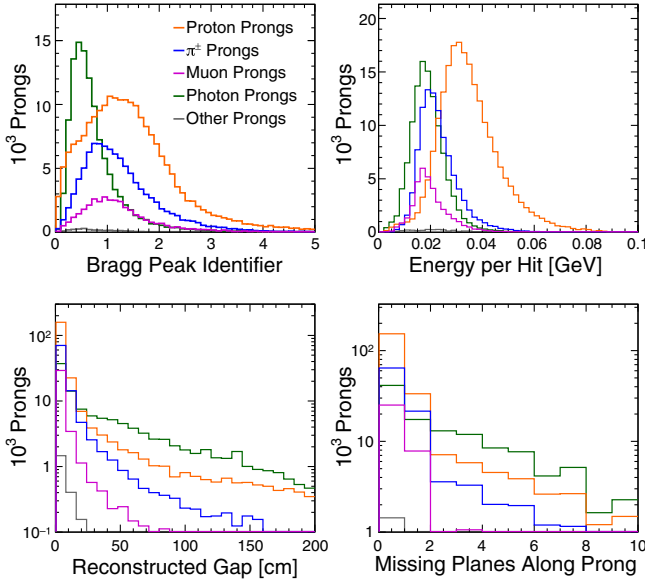
FIG. 2. Simulated distributions of the four variables used to identify photon-induced prongs. (The bottom two panels have logarithmic vertical scales.)

difference in the logarithms of the likelihoods $\Delta \log \mathcal{L}$. An interaction-level score for events with at least two prongs is formed as

$$\mathrm{CC}\pi^0\mathrm{ID} = \max(\Delta \log \mathcal{L}), \tag{2}$$

running over all prongs in the event that are not associated with the muon. That is, the $\mathrm{CC}\pi^0\mathrm{ID}$ score for the event is simply the highest photonlike score among all prongs, neglecting the identified muon prong.

Within an event, the prong that defines the $\mathrm{CC}\pi^0\mathrm{ID}$ value is considered the photon candidate to be associated with the π^0 decay. This photon candidate is used to reconstruct the π^0 kinematics. No attempt is made to reconstruct a second shower from the decay, as doing so gives increased background rates from prong combinatorics in events with significant hadronic activity and gives reduced signal efficiency at higher pion energies due to overlapping or energetically asymmetric photon pairs. According to simulation, requiring a second prong would drop the signal purity to 29% from the current 34%.

C. Reconstruction of event kinematics

The analysis utilizes reconstructed estimates of momentum and of angle with respect to the average beam direction for both the muon and the π^0. The momentum of the π^0 is estimated as the E_{cal} deposited by the single photon candidate prong. This estimator is suitably close to the true π^0 momentum (into which it will ultimately be unfolded) given the predominance of overlapping (merged) or energetically asymmetric photon pairs [33]. The muon momentum is estimated as a linear function of the track
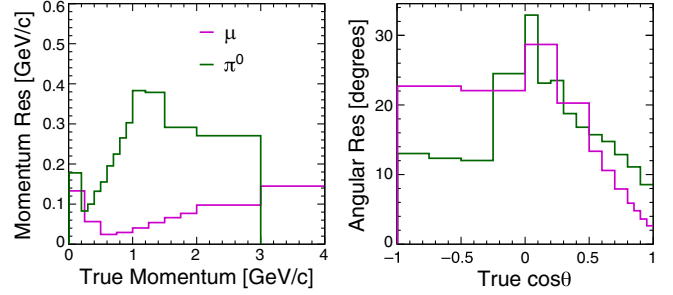

FIG. 3. The absolute momentum (left) and angular (right) resolutions for muons (magenta) and π^0's (green) as predicted by the simulation.

length through the fully instrumented portion of the detector L_1 and through the muon range stack L_2 as

$$p_\mu = c_1 L_1 + c_2 L_2. \tag{3}$$

The constants c_1 and c_2 were determined by optimizing the simulated resolution [34], 3.5% for muon momenta greater than 0.6 GeV/c. The angular resolution is better than $10°$ for $\cos\theta > 0.5$. Muons with larger angles have poorer resolution due to their lower average energies. Those orthogonal to the beam direction ($\cos\theta \approx 0$) are the most difficult to reconstruct due to the detector geometry. The momentum and angular resolutions for π^0's and muons are shown in Fig. 3.

The neutrino energy is reconstructed as

$$E_\nu = E_\mu + E_{\mathrm{Had}}, \tag{4}$$

where E_μ is reconstructed as described above. The reconstructed hadronic energy E_{Had} is determined from the calorimetric energy of all hits except those in the muon track. This estimate includes the E_{cal} estimated from the π^0 candidate. The neutrino energy resolution averaged over the sample is 9.5%.

Differential cross sections in the kinematic variables Q^2 and W are of interest. These quantities are calculated via

$$Q^2 = -(P_\mu - P_\nu)^2 \tag{5}$$

$$= \frac{2E_\nu}{c}\left(\frac{E_\mu}{c} - p_\mu \cos\theta_\mu\right) - m_\mu^2 c^2 \tag{6}$$

and

$$W = \frac{1}{c}|P_N + P_\nu - P_\mu| \tag{7}$$

$$= \frac{1}{c}\sqrt{m_N^2 c^2 - Q^2 + 2m_N(E_\nu - E_\mu)}, \tag{8}$$

where m_N is the nucleon mass, taken numerically here to be the neutron mass, and where P_i is the four-momentum of particle i. Note that p_i here represents the magnitude of the three-momentum of particle i, as it does throughout the

text. This expression assumes the struck target is a stationary nucleon that neglects Fermi motion within the nucleus and neutrino-parton scattering. These kinematic variables as constructed are sensitive to underlying physics. The W variable effectively distinguishes among $\Delta(1232)$ resonance, N^* resonances, and deep-inelastic scattering events. These definitions of Q^2 and W, based on the true final-state kinematics, are used in the cross section definition rather than the event generator's values for these kinematic variables to reduce reliance on the generator's modeling of nuclear structure and FSIs.

D. Event selection

To be analyzed, an interaction must produce a slice in the reconstruction. This requirement removes 2.7% of signal events. Each slice is required to have at least 20 hits and to span at least four planes. Events must also have a reconstructed vertex, track, and at least two reconstructed prongs. The muon track and π^0 candidate prong are then chosen.

Reconstructed vertices are required to lie within a fiducial region defined as a $200 \times 200 \times 900$ cm^3 box centered laterally in the detector and extending between 100 and 1000 cm from the front face. This corresponds to a 35 ton fiducial mass. The fiducial region covers a relatively small fraction of the detector, but ensures efficient containment of tracks. The simulation predicts 2.8×10^5 signal events within the fiducial volume with a purity, defined as the fraction of the simulated sample that is signal, of 11.8% with no further selection criteria applied. There is a leakage of otherwise-selected fiducial CCπ^0 events out of the sample and a spillage of nonfiducial CCπ^0 events into the sample. According to simulation, 2.6% of fiducial events leak out, while 2.8% of the sample are nonfiducial events that spill in. There are no kinematic differences between the leak-out and spill-in events. As these two samples are similar, we treat the nonfiducial CCπ^0 events that leak into the selected sample as signal and thus as a direct compensation for the events that leak out. The efficiency corrections applied in Sec. VI E account for this.

Containment cuts are then applied to ensure reliable reconstruction of the muon and the photon. The photon shower candidate's start and end points as well as the muon's start point are required to be well contained within the fully active portion of the detector. The muon's end point is required to be well contained within any part of the detector including the muon range stack. After containment cuts, the simulated efficiency is 32.8% relative to all fiducial signal interactions, with a simulated purity of 22.6%.

Events are then subject to a convolutional neural network identifier, CVNν_μ [35]. This is a deep learning classifier used to separate ν_μ CC events from the large NC background. Events are required to have CVN$\nu_\mu > 0.5$, which leaves a NC contamination of 1.4% in the selected sample compared to 39.1% before the cut. The distributions
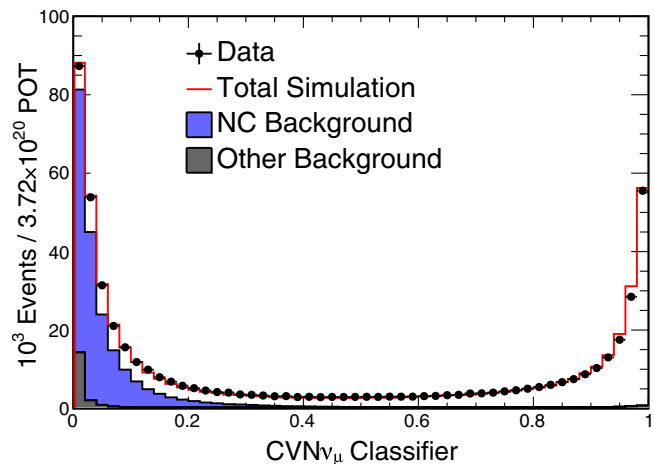

FIG. 4. Comparison of the data and simulation of the convolutional neural-network-based CVNν_μ particle ID. Backgrounds are indicated as shaded subsets of the total. The unshaded portion of the histogram represents ν_μ CC events. Note that the CCπ^0 signal is a subset of the unshaded portion of the histogram.

of CVNν_μ for data and simulation for events at this stage of the selection are shown in Fig. 4.

CVNν_μ also determines whether each event is most likely a quasielastic, resonant, deep-inelastic scattering, or coherent interaction, trained on the GENIE labels for simulated events. Events that CVNν_μ classifies as quasielastic or coherent are also rejected, as these interactions have a well-defined set of final-state particles and do not produce a π^0 except from FSIs. As a cross-check, this cut was replaced with a conventional quasielastic reduction cut by vetoing two-prong events whose measured momenta are consistent with the quasielastic formula. The resulting cross sections agreed to within a percent, and the CVNν_μ cut is used as it more efficiently rejects background.

As noted previously, the photon candidate is required to have a calorimetric energy greater than 100 MeV and at least ten hits to ensure reliable reconstruction. Very loose preselection requirements are also applied on the input variables to CCπ^0ID. These restrictions remove 2.9% of otherwise-selected CCπ^0 events.

Finally, events are removed if any reconstructed values for E_ν, p_π, p_μ, Q^2, and W fail the signal definition conditions laid out in Table I. This restriction removes 0.2% of otherwise-selected CCπ^0 signal events.

In total, the final selected sample consists of CCπ^0 signal (34.4% of the total in the simulation), ν_μ CC events without a π^0 emerging from the nucleus (62.1%), non-ν_μ-CC events including NC events and CC events from other neutrino flavors present in the beam (3.2%), and CCπ^0 events outside the kinematic limits of the signal definition (0.2%). Note that the large background rate of ν_μ CC events is expected in the sample since no explicit cut has been applied at this stage to reject such events. Instead, the

TABLE II. The event counts in data and predicted by simulation at various stages of the selection. All simulated numbers are scaled to the data exposure of 3.72×10^{20} POT. Signal efficiencies are calculated relative to interactions within the true fiducial volume.

Cut	N_{evts}	N_{GENIE}	Efficiency (%)	Purity (%)
Basic reconstruction/ fiducial	2.192×10^6	1.44×10^6	85.1	16.3
Containment	517,317	400,797	32.8	22.6
NC rejection	213,376	197,433	22.2	31.0
QE/coherent rejection	197,858	186,779	22.0	32.7
Prong quality	188,158	175,105	21.3	33.6
Kinematic restriction	164,871	166,980	21.1	34.4

$CC\pi^0$ID event classifier is used to statistically separate signal and background in a fit to the classifier distribution, as described below.

The total selected event counts at each stage of the selection in data and simulation are shown in Table II. At the data exposure of 3.72×10^{20} POT, there are 166,980 predicted and 164,871 observed events. The simulated $CC\pi^0$ID distribution is plotted in Fig. 5 after all selection cuts. The overall signal efficiency is 21% and the purity is 34%, according to simulation. The efficiency and purity as a function of the π^0 and μ^- kinematics are shown in Fig. 6. The efficiency drops sharply to 2.72% below 0.25 GeV/c compared to 27.9% for $0.25 < p_\mu < 0.5$ GeV/c due to difficulty in reconstructing short tracks and in $\mu^-/\pi^\pm$ discrimination. Thus, the differential cross section for $p_\mu < 0.25$ GeV/c is not reported. But, since only 0.5% of selected events have $p_\mu < 0.25$ GeV/c, these events are not removed or treated as background when presenting cross section results in any other kinematic variable.
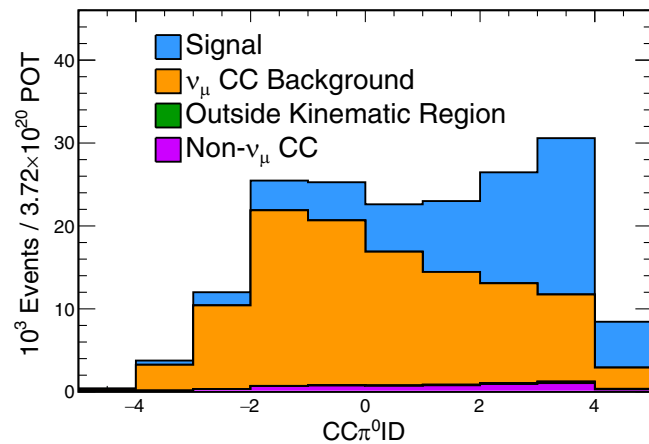

FIG. 5. The $CC\pi^0$ID distribution for all selected events in the simulation, showing clear discrimination between signal and backgrounds. Backgrounds are primarily ν_μ CC events, with small contributions from non-ν_μ-CC events and $CC\pi^0$ events that fail the true kinematic restrictions.
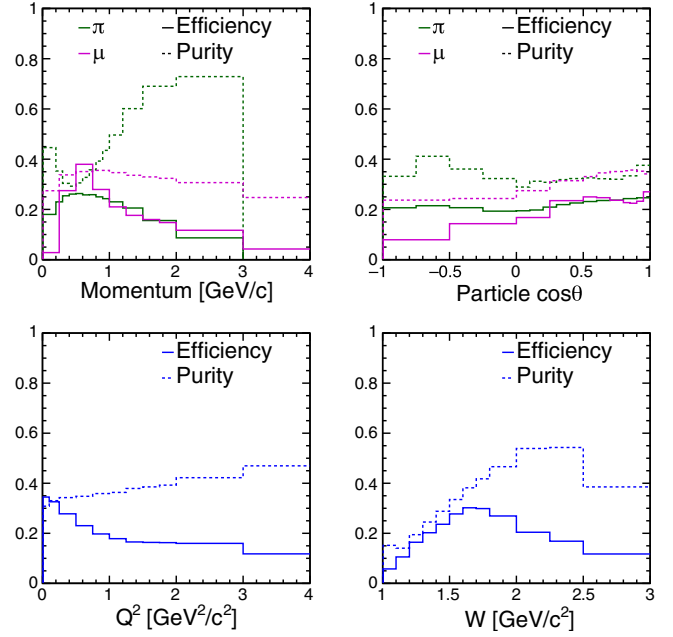

FIG. 6. The event selection efficiency (solid) and purity (dashed) curves as a function of each measured variable. The top plots show the particle momentum (left) and polar angle (right) with magenta and green curves describing the muon and π^0 kinematics, respectively. The bottom plots give the efficiency and purity as a function of Q^2 (left) and W (right).

VI. CROSS SECTION ANALYSIS

Flux-averaged cross sections differential in final-state kinematic variables are presented below. Cross sections are extracted in bins of the true final-state-based kinematic variables. These are defined by the equation

$$\left(\frac{d\sigma}{dx}\right)_i = \frac{(U(\hat{S}))_i}{\Phi N_T \epsilon_i \Delta x_i}. \tag{9}$$

Here, x is the kinematic variable of interest, i is the bin index, Φ is the integrated flux through the detector, N_T is the number of interaction targets, ϵ_i is the detection efficiency in the bin, and Δx_i is the bin width. $\hat{S}$ is a histogram that gives the signal estimate, using simulation constrained by data, in reconstructed bins of x. U refers to an unfolding procedure (described in Sec. VIB), which corrects for smearing effects and any estimator bias in the kinematic reconstruction process.

A. Constraint on simulated signal

As shown in Fig. 5, the $CC\pi^0$ID distributions for the $CC\pi^0$ signal and various categories of background each have their own distinctive shape. The signal and background normalizations are thus determined via a fit of the $CC\pi^0$ID distributions to the observed data. The fit is performed in each kinematic bin independent of other bins. Of the three background categories, the non-ν_μ-CC
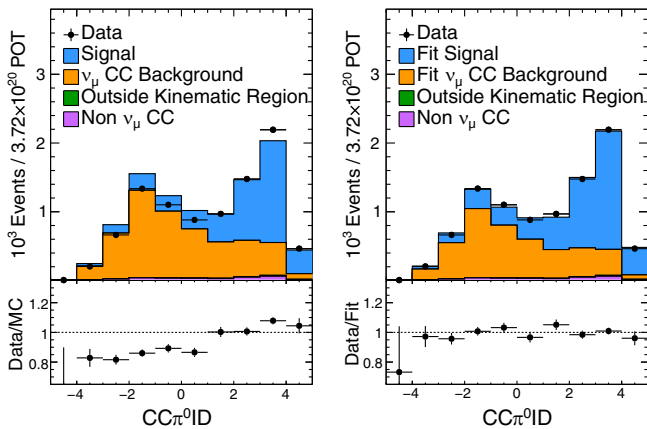
FIG. 7. An example fit to data in $CC\pi^0 ID$ for events reconstructed with $0.8 < p_\pi < 1.0$ GeV/c. Left: compares the unconstrained Monte Carlo (MC) simulated $CC\pi^0 ID$ distribution and data. Right: simulation after constraining signal and background normalizations.

background and the background of $CC\pi^0$ that fail the kinematic requirements are both held fixed in the fit since they represent small populations, at 3.2% and 0.2%, respectively. The remaining (ν_μ CC) background and signal normalizations are fit to the observed data distributions. The signal and background normalizations float independently and without penalty. As an example, the $CC\pi^0 ID$ distribution is shown in Fig. 7 for events in a representative bin of p_π before and after fitting to data.

B. Signal unfolding

For each variable of interest, an unfolding procedure is applied to correct for reconstruction effects and thus to obtain an estimate of each variable's true distribution. The simulated true-to-reconstructed migration matrix for the variable is used as input to the unfolding. Several unfolding procedures were considered, with a two-iteration D'Agostini [36,37] technique ultimately being selected given its excellent robustness to the dominant analysis uncertainties, as demonstrated using sets of systematically fluctuated fake data.

C. Nuclear target count

Since the NOvA detector consists of a mixture of materials, the result is presented as a cross section per nucleon. The list of constituent elements is shown in Table III. The detector is largely CH_2 with notable portions of oxygen, chlorine, and titanium, with $\langle A \rangle = 15.96$. The mass of the fiducial volume is 35,430 kg with a nucleon count of 2.12×10^{31}. This is known to better than 1%, as described in Sec. VII A.

D. Integrated flux

As described in Sec. III A, the NuMI flux simulation is constrained with external hadron-production data using the

TABLE III. The mass of the fiducial volume, broken down by element. Trace amounts of nitrogen, sodium, sulphur, calcium, and tin are present and accounted for in simulation.

Element	Mass (kg)	Nucleon count	Mass fraction
H	3814.5	2.28×10^{30}	0.108
C	23,650	1.41×10^{31}	0.667
O	1050	6.30×10^{29}	0.030
Cl	5690	3.40×10^{30}	0.161
Ti	1140	6.81×10^{29}	0.032
Other	95	5.7×10^{28}	0.003

PPFX package [16]. The integrated flux through the detector in the analyzed energy range is 87.0 $\nu_\mu/\text{cm}^2/10^{10}$ POT.

E. Efficiency correction

Selection efficiencies for each of the variables are calculated with the simulation as a function of the true kinematics, shown in Fig. 6. The efficiency is defined as the ratio of selected signal events to the true number of signal events generated in the fiducial volume. For the purposes of this calculation, the fiducial volume cut in the selection is truth based rather than reconstruction based to account for the compensation for those events that nominally leak out of the fiducial volume, as discussed in Sec. V D.

VII. SYSTEMATIC UNCERTAINTY

Several sources of systematic uncertainty are considered, classified into five separate groups: event normalization, neutrino flux, neutrino cross sections, uncertainty in the $\pi^\pm \to \pi^0$ CX cross section, and detector response. For each source of uncertainty within these categories, cross section covariance matrices are determined by repeating the cross section measurement many times using an ensemble of altered versions of the simulation, where each alteration takes a random adjustment for the error source of interest chosen from its Gaussian distribution.

The final reported cross section covariance matrices include these systematic uncertainties, as well as (much smaller) statistical uncertainties.

A. Data normalization uncertainties

Three sources contribute to the normalization uncertainty. The fiducial mass, and thus the number of nucleon targets in the fiducial volume, is known to 0.7%. Variation in beam intensity, and thus also event pileup, leads to no more than a 0.5% effect on event reconstruction efficiency, as the event-isolating step of the reconstruction (Sec. V A) is highly effective. A 1.9% uncertainty from modeling of particle containment is calculated by examining the differences of extracted cross sections between the inner and outer halves of the fiducial volume. The uncertainty associated with POT counting and events interacting in the

rock surrounding the detector were calculated but are negligible. The overall normalization uncertainty is 2.1%.

B. Flux uncertainties

Two broad sources of flux systematic uncertainty were assessed. One comes from hadronization during the proton beam's initial collisions with the NuMI target. The PPFX prediction [16] was used to calculate the corresponding uncertainty on the NuMI flux—about 8% near the beam peak. Systematic uncertainties from beam transport were also assessed. These correspond to multiple aspects of the neutrino beamline such as horn current, horn position, proton beam position on the target, beam spot size, and bending from Earth's magnetic field in the decay pipe. These transport effects taken together lead to flux uncertainties around 5% near the beam peak.

C. Neutrino cross section uncertainties

The effect of neutrino interaction uncertainties is calculated using the GENIE event reweighting infrastructure [38]. Only systematic sources producing greater than a 0.5% effect on the selected event rate are explicitly included in the analysis. These include sources that affect GENIE's prediction for resonant and DIS events in the sample and modify the model by which initially produced particles undergo FSIs. The effect of any excluded GENIE systematic parameters was verified to have a negligible impact on the result.

Additionally, GENIE only calculates an uncertainty for DIS events with $W < 2$ GeV/c^2. To treat the remaining DIS events, a 15% normalization uncertainty is added for DIS events at higher W, as motivated by neutrino scattering data [39].

D. Particle tracking cross section uncertainties

According to simulation, about a quarter of the ν_μ CC background events (cf. Fig. 5) contain a secondary π^0 produced via hadronic interactions downstream in the detector, typically through the charge exchange (CX) reaction. Given the importance of this process, a final systematic uncertainty adjusts the simulated cross section for $\pi^\pm \to \pi^0$ CX. To bring in the most recent measurements of the CX cross section, the central value and error band used in this analysis were determined by fitting data from the DUET experiment [40]. This dataset offers a factor of 3 more precise cross section than that used to tune Geant4 [41]. The fit increases the cross section by 6.1% relative to the default simulation with a 14.6% error band as shown in Fig. 8. The effect of uncertainty in the shape of this cross section was also studied, but found to be negligible.

E. Detector response uncertainties

Uncertainty in the light yield of the liquid scintillator is assessed by varying scintillator quenching parameters simulated according to the Birks-Chou formula [25,42] given by
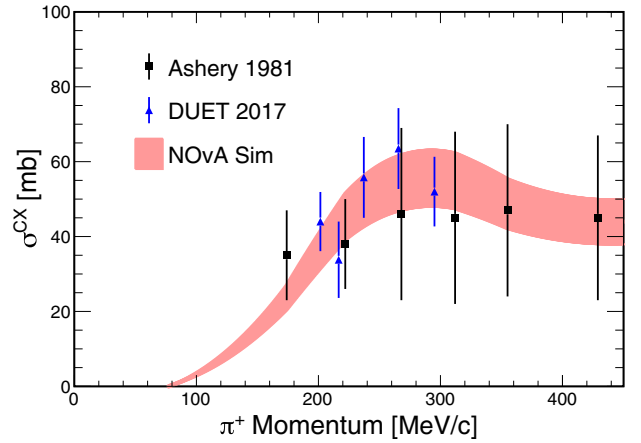

FIG. 8. A comparison of the Ashery *et al.* [41] and DUET [40] measurements of the $\pi^+ \to \pi^0$ CX cross section and the spread in cross section of the NOvA simulation consistent with these results. A 68.3% confidence interval for the range of scale factors applied to the nominal simulation was calculated as 1.061 ± 0.146 from a fit to the DUET data.

$$LY = A \frac{\frac{dE}{dx}}{1 + k_B \frac{dE}{dx} + k_C (\frac{dE}{dx})^2}. \qquad (10)$$

The Birks-Chou parameters were fit to data using the dE/dX of stopping protons whose track length was greater than 1 m. This fit produced an anomalously high value $k_B = 0.046$ cm/MeV with $k_C = -0.00058$ cm^2/MeV^2, versus typical values for organic liquid scintillators of $k_B \approx 0.01$ cm/MeV. Borexino measured $k_B = 0.01055$ cm/MeV [43] in a similar scintillator blend to NOvA's. The discrepancy is explained by the lack of a Cherenkov light component in the default simulation. (Studies using a later version of the NOvA simulation that includes Cherenkov light yield $k_B = 0.012$ cm/MeV with $k_C = 0$.) To compensate for this known shortcoming of the simulation used here, a systematic uncertainty was calculated by taking the difference in the cross sections determined using the default simulation and a shifted simulation that assumes $k_B = 0.012$ cm/MeV.

A set of detector calibration uncertainties are also included. One class of uncertainties varies the energy of the photon candidate by 2% and the remaining hadronic energy by 5%. The hadronic energy uncertainty originates from a comparison of the simulated dE/dx profile of stopping protons to data. The photon energy uncertainty is determined by data/simulation comparisons of electrons from muon decay. For photons, an additional gauge of the quality of the energy scale calibration is provided by the π^0 invariant mass, as reconstructed using a subset of the CCπ^0 sample with only three reconstructed particles consistent with a $\mu^-\gamma\gamma$ topology. As shown in Fig. 9, the peak of the mass spectrum observed in data lies within 1% of the simulated peak, well within the assessed 2% energy scale uncertainty.
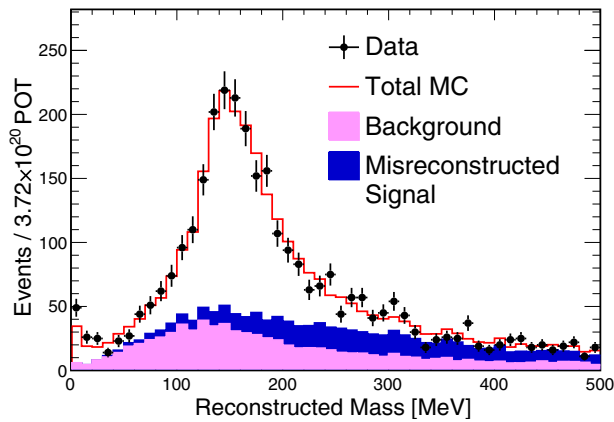
FIG. 9. The reconstructed π^0 mass from the small subsample of fully reconstructed $\mu\gamma\gamma$ candidate events.

FIG. 10. The CCπ^0ID distribution for a control sample of photons (left) and protons (right). Simulation and data have been area normalized to suppress overall normalization uncertainties. Each bottom panel shows the ratio of data to simulation, with an error band from detector response uncertainties.

A separate calibration uncertainty relates to the spatial variation in the collection and transport of light from energy depositions at various positions along the length of a detector cell. While this uncertainty has a much smaller effect on the resulting cross section measurement, its impact is not completely negligible in some regions of kinematic space, and thus it is included throughout.

F. Tests of the estimated detector response error band

High-purity samples of photons and protons were developed to test the estimated detector response systematic error band. Photons are selected from a high-purity sample of two-prong NCπ^0 events. Both prongs are required to have dE/dx, reconstructed energy gaps, and prong length consistent with a photon. Additionally, the reconstructed invariant mass must lie near m_{π^0}. This selection gives an 82.1% pure sample of photons. Protons are selected in two-prong events that pass a ν_μ CC selection [44]. To identify events whose secondary prong was a proton, first, the reconstructed angle between the muon and proton candidate prongs must have $\cos\theta_{\mu p} > -0.8$ to remove a reconstruction failure that can split a muon track into two by misreconstructing the vertex. Second, the proton direction inferred from the quasielastic formula [45] using only the observed muon kinematics is required to be coincident with the observed prong direction; the criterion is $\hat{\mathbf{p}}_p^{pr} \cdot \hat{\mathbf{p}}_p^{\mathrm{QE}} > 0.9$, where $\hat{\mathbf{p}}_p^{pr}$ is the unit vector proton direction determined by the prong reconstruction and $\hat{\mathbf{p}}_p^{\mathrm{QE}}$ is that determined using the quasielastic formula. This gives an 82.9% pure sample of protons.

An area-normalized comparison of CCπ^0ID in data and simulation with shape-only detector response systematic errors for these two samples is shown in Fig. 10. The differences observed between data and simulation lie well within the estimated error band, offering a level of confirmation that the systematic treatment adequately addresses the relevant uncertainties in the response of CCπ^0ID to signal particles and the most important backgrounds.
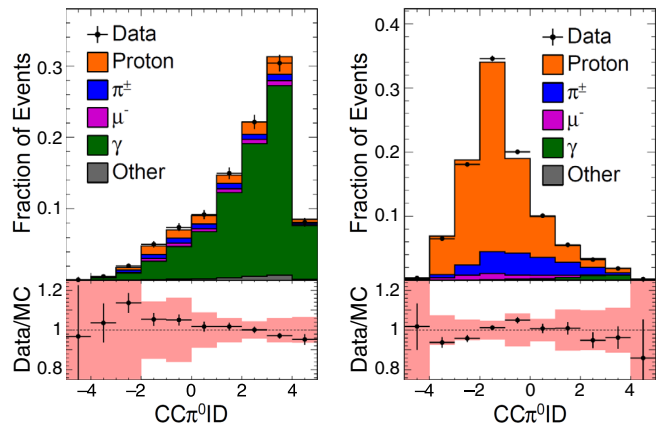
G. Total systematic uncertainty

The total systematic error, as a function of measured p_π and Q^2, is shown in Fig. 11. The systematic uncertainty on the total cross section, broken down by each source, is shown in Table IV.

FIG. 11. The systematic uncertainty budget as a function of π^0 momentum (top) and Q^2 (bottom). No single uncertainty source dominates the overall measurement uncertainty throughout the whole kinematic range.

TABLE IV. The effect of each systematic uncertainty on the extracted total cross section. The flux uncertainties are the largest source of systematic error, with large contributions from the light level, calibration, $\pi^{\pm}$ charge exchange, and the neutrino interaction model.

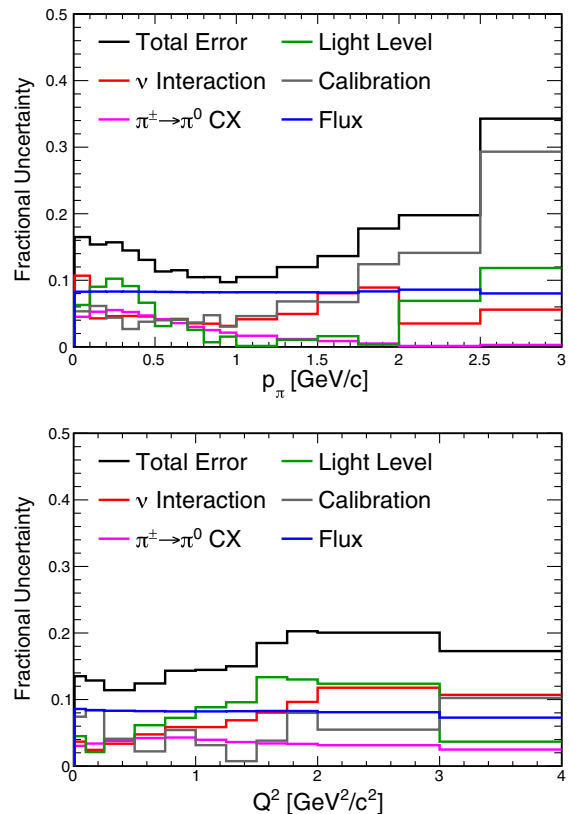| Systematic source	Relative error (%)
Normalization	2.1
Flux	8.3
Neutrino interaction model	4.6
$\pi^{\pm}$ charge exchange	3.8
Light level	6.8
Calibration	2.6
Quadrature sum	12.5

VIII. ANALYSIS RESULTS

The sections that follow discuss the measured differential cross sections in each kinematic variable and the total cross section, with comparisons to the reference GENIE
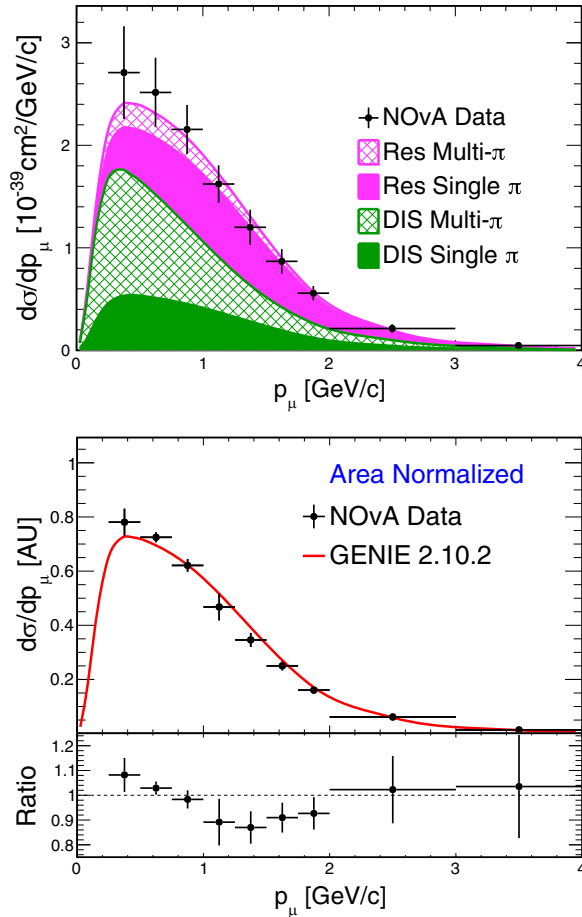
model throughout. In general, a 7.5% larger total cross section is observed compared to the GENIE prediction, though results are within the systematic error associated with flux normalization.

A. Muon kinematics

The measured differential cross sections in p_μ and $\cos\theta_\mu$, along with the GENIE predictions, are shown in Figs. 12 and 13, respectively. The predictions are separated into contributions from resonant and DIS scattering along with pion multiplicity. Averaged over the flux, multi-π interactions account for 48% of the predicted total cross section. Multi-π events are more dominant at low p_μ, where ν_μ CC background events are more likely to be selected in ν_e oscillation measurements. The cross section for $p_\mu < 0.25$ GeV/c is not reported due to the low efficiency for reconstructing and tagging short muon tracks. GENIE predicts that this region represents 4% of the total cross section and is primarily populated by DIS multi-π interactions.

In the lower panels, the simulation is rescaled so that the integrated cross section matches the measurement, which allows trends in the comparison to be more readily observed.

FIG. 12. The measured absolute differential cross section (top) and area-normalized differential cross section (bottom), per nucleon, vs p_μ. For the absolute cross section, the GENIE prediction is shown separated into resonant and DIS production and by π multiplicity. Bottom: the ratio of the measured cross section to the GENIE prediction is also shown in a subpanel.
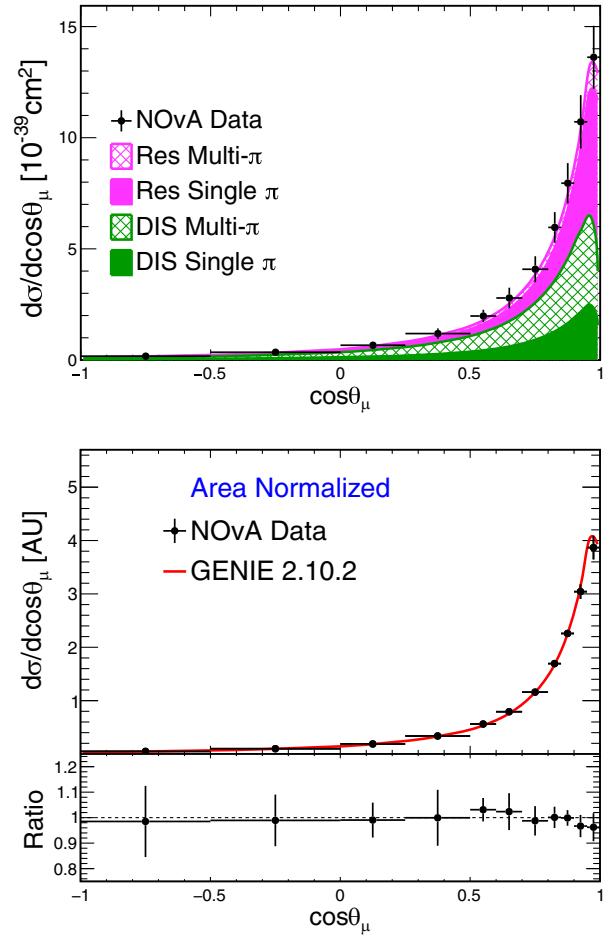

FIG. 13. As in Fig. 12, but for $\cos\theta_\mu$.

A χ^2 can be calculated for this result to explore the level of agreement between the measured and GENIE-predicted cross sections,

$$\chi^2 = \sum d_i M_{ij}^{-1} d_j, \qquad (11)$$

where d_i is the difference between measured and predicted cross sections in bin i and M_{ij}^{-1} is an element of the inverse of the covariance matrix. The sum runs over all bins in the kinematic variable of interest. The area scaling applied for visualization purposes above is not used here. We calculate $\chi^2/\text{d.o.f.} = 9.75/9$ for the differential cross section in p_μ and $\chi^2/\text{d.o.f.} = 5.26/11$ for the differential cross section in $\cos\theta_\mu$.

B. π^0 kinematics

The differential cross sections in the π^0 kinematic variables are shown in Figs. 14 and 15, with predictions separated into final-state interaction channels. In the
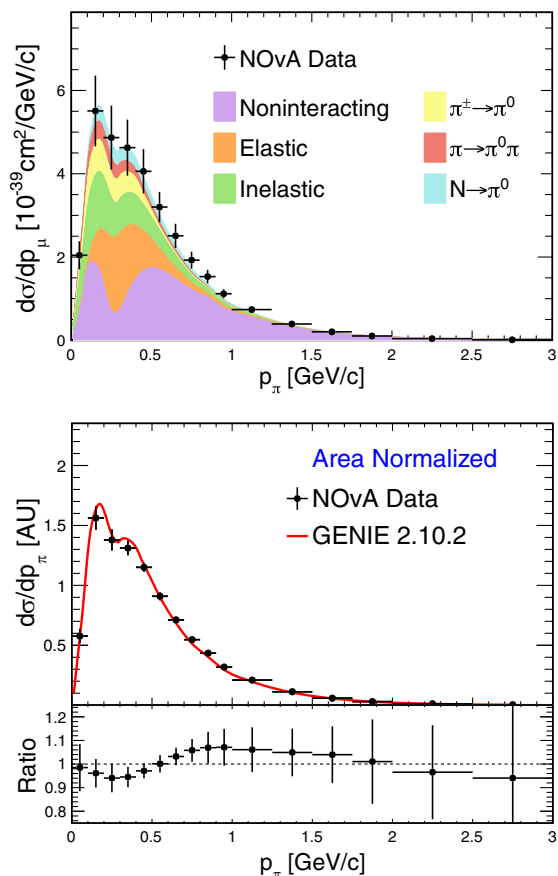

FIG. 14. The measured absolute differential cross section (top) and area-normalized differential cross section (bottom), per nucleon, vs p_π. For the absolute cross section, the GENIE prediction is shown separated according to FSI channel; the $\pi + p \to \Delta(1232)$ resonance occurs around $p_\pi = 0.3$ GeV/c. Bottom: the ratio of the measured cross section to the GENIE prediction is also shown in a subpanel.
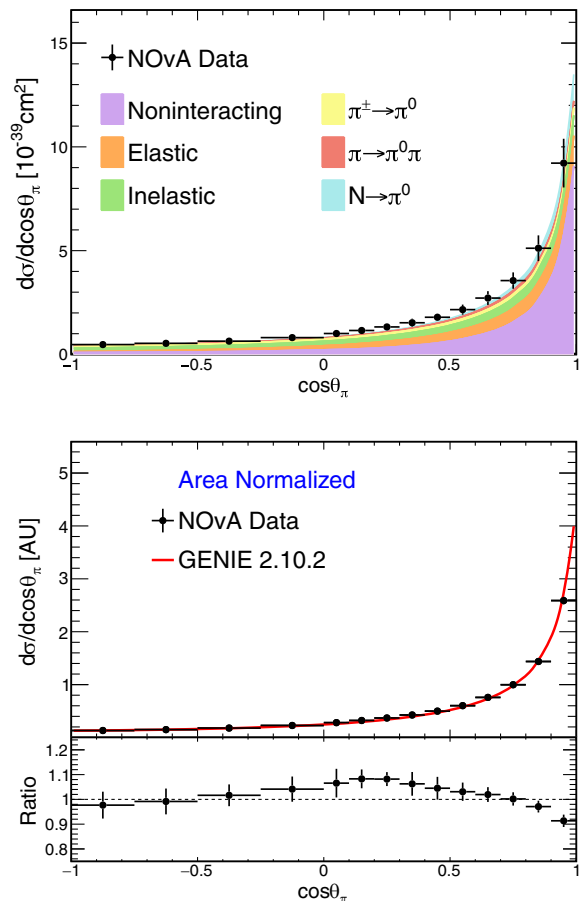
FIG. 15. As in Fig. 14, but for $\cos\theta_\pi$.

simulation, the majority of pions below ~ 0.5 GeV/c are involved in some sort of final-state interaction, and a subset of these involve production of a π^0 (namely, the latter three FSI categories shown in the figures, corresponding to pion charge exchange, pion-induced π^0 production, and nucleon-induced π^0 production).

The p_π comparison yields a $\chi^2/\text{d.o.f.} = 21.49/16$. There is a slight preference for a higher-momentum distribution in data, though consistent with the simulation given the uncertainty. In the predicted p_π differential cross section there is a clear dip near $p_\pi = 0.3$ GeV/c. This stems primarily from $\pi + p \to \Delta(1232)$ resonance production, which is modeled in GENIE alongside a number of other resonances and intranuclear hadronic processes.

For $\cos\theta_\pi$, a $\chi^2/\text{d.o.f.} = 32.12/14$ is calculated, with tension both in the $0 < \cos\theta_\pi < 0.5$ region and in the very forward-going direction. Such a flattening of the peak could be evidence for stronger FSI than predicted by GENIE, though angular differences between DIS and resonant scattering, for instance, also influence this region.

C. Q^2 and W

Results in Q^2, shown in Fig. 16, agree well with predictions with $\chi^2/\text{d.o.f.} = 11.33/11$. The prediction

FIG. 16. The measured absolute differential cross section (top) and area-normalized differential cross section (bottom), per nucleon, vs Q^2. For the absolute cross section, the GENIE prediction is shown separated into $\Delta(1232)$ resonance, N^* resonances, and DIS contributions. Bottom: the ratio of the measured cross section to the GENIE prediction is also shown in a subpanel.

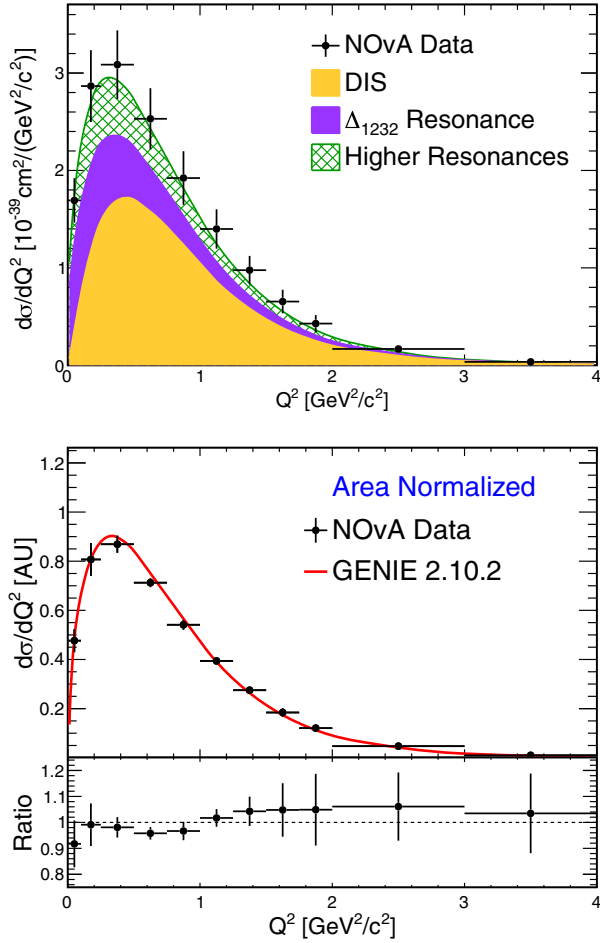FIG. 17. As in Fig. 16, but for W.

has been divided into contributions from DIS (60% of total cross section), the $\Delta(1232)$ resonance (22%), and higher N^* resonances (18%). This variable has shown sharp disagreements in past results [6] when looking at single-π events with very forward $\cos\theta_\mu$.

The shape of the W distribution (Fig. 17) is relatively well modeled, with $\chi^2/\text{d.o.f.} = 13.29/12$, particularly compared to other available W measurements in semi-inclusive meson-production measurements in other energy ranges [6,8]. Notably, the observed shape is in agreement with GENIE for masses between 1.3 and 1.7 GeV/c^2, exactly the region where GENIE predicts that N^* resonances more massive than $\Delta(1232)$ contribute significantly to the cross section. This version of GENIE does not include interference effects between the various pion-production channels [46].

D. Total flux-averaged $CC\pi^0$ cross section

The total cross section determined by integrating the differential cross section in each kinematic variable is slightly different for each variable. The reported total cross section is determined by averaging the total cross section obtained from the individual differential cross sections. The differential cross section in p_μ is not included in the average as it is reported only for $p_\mu > 0.25$ GeV/c. The spread in individually measured cross sections is much smaller than the total cross section error, as shown in Table V.

TABLE V. The total cross section and error as determined from each differential result.

Kinematic variable	$\langle\sigma\rangle_\Phi (10^{-39}\ \text{cm}^2)$
p_π	3.53 ± 0.42
$\cos\theta_\pi$	3.57 ± 0.42
$\cos\theta_\mu$	3.52 ± 0.43
Q^2	3.55 ± 0.44
W	3.68 ± 0.43
GENIE	3.32

The average total cross section is $(3.57 \pm 0.44) \times 10^{-39}$ cm^2/nucleon.

IX. CONCLUSION

A set of systematically limited measurements of π^0-production kinematics in ν_μ CC events has been presented. The measured total cross section is 7.5% higher than the GENIE prediction but consistent within experimental error. The studied energy region directly overlaps the transitional energy range between QE- and DIS-dominated scattering regimes so that baryon resonance and DIS events both contribute to the studied signal. This energy region is particularly relevant for current and future oscillation measurements. The signal definition for the measurement includes multi-π events, which have been shown to cause the majority of π^0 background events in $\nu_\mu \to \nu_e$ oscillation measurements in NOvA.

Detailed numerical tables of the NOvA flux and the extracted cross sections with covariances are included in the Appendices in Tables VI–XII.

ACKNOWLEDGMENTS

APPENDIX A: NEUTRINO FLUX IN THE NuMI BEAM

TABLE VI. The neutrino flux through the NOvA ND in bins of energy. Histogram entries are normalized to 10^{10} POT incident on the NuMI target.

Energy range (GeV)	Flux (ν/cm^2/10^{10} POT)	Energy range (GeV)	Flux (ν/cm^2/10^{10} POT)
1.0–1.1	2.143	3.0–3.1	0.766
1.1–1.2	2.462	3.1–3.2	0.601
1.2–1.3	2.994	3.2–3.3	0.455

(Table continued)

TABLE VI. *(Continued)*

Energy range (GeV)	Flux (ν/cm^2/10^{10} POT)	Energy range (GeV)	Flux (ν/cm^2/10^{10} POT)
1.3–1.4	3.896	3.3–3.4	0.367
1.4–1.5	4.712	3.4–3.5	0.304
1.5–1.6	5.405	3.5–3.6	0.263
1.6–1.7	6.129	3.6–3.7	0.256
1.7–1.8	6.670	3.7–3.8	0.225
1.8–1.9	6.969	3.8–3.9	0.214
1.9–2.0	7.050	3.9–4.0	0.195
2.0–2.1	6.728	4.0–4.1	0.183
2.1–2.2	6.041	4.1–4.2	0.177
2.2–2.3	5.093	4.2–4.3	0.180
2.3–2.4	4.060	4.3–4.4	0.149
2.4–2.5	3.238	4.4–4.5	0.148
2.5–2.6	2.508	4.5–4.6	0.153
2.6–2.7	1.976	4.6–4.7	0.128
2.7–2.8	1.554	4.7–4.8	0.127
2.8–2.9	1.227	4.8–4.9	0.128
2.9–3.0	0.975	4.9–5.0	0.127

APPENDIX B: MEASURED DIFFERENTIAL CROSS SECTION TABLES

TABLE VII. A summary of the extracted CCπ^0 cross section, differential in p_μ. The top row and the left column give the lower edges of each analysis bin. The second row gives the central value of the cross section measurement in 10^{-40} cm^2/(GeV/c) for each kinematic bin, while the third row gives the GENIE prediction. The remaining matrix gives covariance and correlation information. Entries in the upper right and along the diagonal are covariances in units of 10^{-80} cm^4/(GeV/c)^2, while entries in the lower left are dimensionless correlation coefficients. All entries correspond to absolutely normalized results. Area-normalized results that appear elsewhere in the text are presented only for those specific visualization purposes.

	0.00	0.25	0.50	0.75	1.00	1.25	1.50	1.75	2.00	3.00
$\frac{d\sigma}{dp_\mu}$	···	27.1	25.2	21.6	16.2	12.0	8.68	5.57	2.13	0.47
GENIE	10.8	23.7	23.1	20.7	17.2	13.0	9.03	5.69	1.97	0.43
0.00	···	···	···	···	···	···	···	···	···	···
0.25	···	17.2	12.4	8.17	3.45	4.98	3.64	1.84	1.05	0.32
0.50	···	0.95	9.96	6.58	2.83	4.09	3.14	1.57	0.95	0.28
0.75	···	0.89	0.94	4.92	2.45	3.03	2.17	1.14	0.61	0.17
1.00	···	0.49	0.53	0.65	2.86	0.85	0.62	0.44	0.10	−0.03
1.25	···	0.72	0.78	0.82	0.30	2.77	1.76	0.91	0.51	0.16
1.50	···	0.72	0.82	0.80	0.30	0.87	1.48	0.67	0.42	0.13
1.75	···	0.67	0.75	0.78	0.39	0.82	0.82	0.44	0.21	0.06
2.00	···	0.64	0.76	0.69	0.15	0.78	0.88	0.80	0.15	0.05
3.00	···	0.45	0.52	0.46	−0.11	0.58	0.61	0.53	0.68	0.03

TABLE VIII. Same as in Table VII, but for $\cos\theta_\mu$ with cross section units of 10^{-40} cm^2 and covariance units of 10^{-80} cm^4.

	−1.00	−0.50	0.00	0.25	0.50	0.60	0.70	0.80	0.85	0.90	0.95
$\frac{d\sigma}{d\cos\theta_\mu}$	1.72	3.49	6.64	11.9	19.8	27.9	40.8	59.6	79.5	107	136
GENIE	1.63	3.29	6.25	11.1	17.9	25.4	38.5	55.5	74.2	103	132
−1.00	0.16	0.25	0.46	0.77	0.95	1.61	1.78	2.11	2.95	3.92	3.51
−0.50	0.97	0.42	0.74	1.19	1.45	2.46	2.93	3.52	4.83	6.35	5.71
0.00	0.93	0.93	1.51	2.92	3.32	5.77	6.14	7.00	9.95	13.1	12.4
0.25	0.73	0.70	0.90	7.03	7.19	13.1	11.3	12.4	18.9	25.3	25.4
0.50	0.76	0.72	0.87	0.87	9.73	14.5	15.2	17.6	25.8	34.7	36.9
0.60	0.79	0.75	0.93	0.97	0.92	25.8	24.0	27.2	40.6	54.1	55.8
0.70	0.77	0.78	0.87	0.74	0.85	0.82	33.4	37.1	50.1	61.8	66.9
0.80	0.78	0.80	0.84	0.69	0.83	0.79	0.95	45.9	59.8	75.4	82.5
0.85	0.79	0.80	0.87	0.77	0.89	0.86	0.93	0.95	86.4	111	123
0.90	0.77	0.77	0.84	0.75	0.88	0.84	0.84	0.88	0.94	161	160
0.95	0.61	0.62	0.71	0.67	0.83	0.77	0.81	0.85	0.93	0.88	203

TABLE IX. Same as in Table VII, but for p_π.

	0.00	0.10	0.20	0.30	0.40	0.50	0.60	0.70	0.80	0.90	1.00	1.25	1.50	1.75	2.00	2.50
$\frac{d\sigma}{dp_\pi}$	20.3	55.1	48.6	46.2	40.6	32.0	25.1	19.3	15.3	11.2	7.39	3.95	2.07	1.05	0.41	0.12
GENIE	19.2	53.3	48.1	45.5	38.9	29.8	22.6	17.0	13.3	9.75	6.48	3.50	1.85	0.97	0.40	0.12
0.00	11.3	22.0	17.0	14.2	10.6	7.59	5.76	3.99	2.69	1.71	0.90	0.41	0.19	0.70	−0.013	−0.029
0.10	0.80	67.6	59.2	49.5	35.0	21.8	16.9	10.7	6.78	4.04	1.77	0.82	0.44	−0.008	−0.15	−0.15
0.20	0.68	0.96	55.8	46.8	32.5	19.4	15.3	9.44	5.83	3.63	1.56	0.83	0.55	0.08	−0.12	−0.138
0.30	0.65	0.93	0.96	42.3	30.1	18.4	14.5	9.11	5.80	3.75	1.85	1.10	0.70	0.23	−0.05	−0.09
0.40	0.65	0.88	0.90	0.95	23.6	15.2	11.9	7.63	5.25	3.19	1.81	1.06	0.63	0.23	0.02	−0.04
0.50	0.68	0.79	0.78	0.85	0.94	11.1	8.22	5.59	4.11	2.41	1.52	0.84	0.48	0.19	0.05	−0.02
0.60	0.67	0.80	0.80	0.87	0.95	0.96	6.62	4.32	3.13	1.95	1.23	0.70	0.37	0.17	0.05	−0.005
0.70	0.68	0.74	0.72	0.80	0.90	0.96	0.96	3.06	2.25	1.42	0.93	0.50	0.26	0.11	0.04	−0.005
0.80	0.59	0.61	0.58	0.66	0.80	0.91	0.90	0.95	1.83	1.09	0.78	0.43	0.23	0.11	0.04	0.004
0.90	0.56	0.54	0.54	0.64	0.72	0.80	0.84	0.90	0.89	0.82	0.54	0.306	0.16	0.09	0.03	0.005
1.00	0.42	0.33	0.33	0.44	0.58	0.71	0.74	0.82	0.89	0.93	0.41	0.24	0.13	0.07	0.03	0.009
1.25	0.30	0.24	0.27	0.41	0.53	0.61	0.66	0.70	0.76	0.81	0.91	0.17	0.10	0.06	0.02	0.009
1.50	0.21	0.20	0.27	0.39	0.47	0.53	0.53	0.54	0.62	0.65	0.74	0.85	0.08	0.04	0.01	0.005
1.75	0.12	−0.01	0.06	0.19	0.27	0.32	0.37	0.36	0.44	0.56	0.65	0.78	0.82	0.03	0.01	0.005
2.00	−0.05	−0.24	−0.23	−0.10	0.04	0.20	0.24	0.28	0.42	0.44	0.65	0.72	0.61	0.77	0.005	0.003
2.50	−0.16	−0.36	−0.35	−0.27	−0.16	−0.09	−0.04	−0.06	0.06	0.11	0.28	0.42	0.35	0.57	0.72	0.003

TABLE X. Same as in Table VII, but for $\cos\theta_\pi$ with cross section units of 10^{-40} cm^2 and covariance units of 10^{-80} cm^4.

	−1.00	−0.75	−0.50	−0.25	0.00	0.10	0.20	0.30	0.40	0.50	0.60	0.70	0.80	0.90
$\frac{d\sigma}{d\cos\theta_\pi}$	4.73	5.32	6.39	8.12	10.0	11.5	13.2	15.2	17.8	21.5	27.1	35.6	51.3	92.5
GENIE	4.45	4.93	5.77	7.17	8.66	9.76	11.2	13.2	15.7	19.2	24.4	32.7	4.86	93.1
−1.00	0.48	0.57	0.67	0.74	1.05	0.94	1.13	1.23	1.04	1.54	2.09	2.49	4.07	7.56
−0.75	0.97	0.73	0.82	1.88	1.31	1.45	1.41	1.57	1.29	1.93	2.65	3.03	4.92	9.27
−0.50	0.96	0.95	1.01	1.03	1.56	1.35	1.66	1.88	1.48	2.27	3.18	3.59	5.85	11.2
−0.25	0.98	0.94	0.94	1.20	1.66	1.51	1.76	1.93	1.66	2.45	3.25	3.92	6.28	11.5

(Table continued)

TABLE X. *(Continued)*

	−1.00	−0.75	−0.50	−0.25	0.00	0.10	0.20	0.30	0.40	0.50	0.60	0.70	0.80	0.90
$\frac{d\sigma}{d\cos\theta_\pi}$	4.73	5.32	6.39	8.12	10.0	11.5	13.2	15.2	17.8	21.5	27.1	35.6	51.3	92.5
GENIE	4.45	4.93	5.77	7.17	8.66	9.76	11.2	13.2	15.7	19.2	24.4	32.7	4.86	93.1
0.00	0.92	0.93	0.95	0.93	2.69	2.20	2.61	3.07	2.29	3.69	5.02	5.52	8.84	17.0
0.10	0.95	0.95	0.95	0.97	0.95	2.01	2.35	2.70	2.23	3.37	4.47	5.18	8.11	15.3
0.20	0.95	0.96	0.96	0.93	0.93	0.97	2.95	3.29	2.76	4.08	5.60	6.41	10.2	19.4
0.30	0.87	0.91	0.92	0.87	0.92	0.94	0.94	4.11	3.09	4.89	6.63	7.12	10.9	21.7
0.40	0.87	0.87	0.85	0.87	0.80	0.91	0.93	0.88	3.02	4.03	5.35	6.42	9.80	18.42
0.50	0.88	0.90	0.90	0.89	0.90	0.95	0.95	0.96	0.92	6.30	8.17	9.23	14.0	27.3
0.60	0.90	0.92	0.94	0.88	0.91	0.94	0.97	0.97	0.92	0.97	11.3	12.4	19.3	38.0
0.70	0.92	0.91	0.92	0.92	0.86	0.94	0.96	0.90	0.95	0.95	0.95	15.1	23.4	44.2
0.80	0.95	0.93	0.94	0.93	0.87	0.93	0.96	0.87	0.91	0.90	0.93	0.98	38.1	71.0
0.90	0.93	0.92	0.95	0.90	0.88	0.92	0.96	0.91	0.90	0.93	0.96	0.97	0.98	138

TABLE XI. Same as in Table VII, but for Q^2 with cross section units of 10^{-40} cm^2/(GeV/c)^2 and covariance units of 10^{-80} cm^4/(GeV/c)^4.

	0.00	0.10	0.25	0.50	0.75	1.00	1.25	1.50	1.75	2.00	3.00
$\frac{d\sigma}{dQ^2}$	16.9	28.7	30.9	25.3	19.2	14.0	9.76	6.54	4.28	1.68	0.35
GENIE	17.1	26.8	29.1	24.4	18.4	12.7	8.66	5.77	3.77	1.46	0.31
0.00	5.03	6.58	6.77	5.11	4.33	3.27	2.07	1.31	0.69	0.30	−0.008
0.10	0.82	12.8	11.3	8.57	8.16	5.52	3.05	1.89	1.02	0.46	0.002
0.25	0.85	0.88	12.7	11.4	9.67	7.18	4.81	3.53	2.27	0.91	0.08
0.50	0.66	0.69	0.92	12.0	9.56	7.35	5.31	4.23	2.90	1.13	0.14
0.75	0.66	0.78	0.92	0.94	8.61	6.22	4.27	3.35	2.18	0.88	0.09
1.00	0.66	0.69	0.91	0.96	0.96	4.93	3.42	2.77	1.79	0.72	0.07
1.25	0.56	0.52	0.82	0.94	0.89	0.94	2.67	2.15	1.47	0.58	0.07
1.50	0.43	0.39	0.72	0.89	0.83	0.91	0.96	1.88	1.26	0.49	0.06
1.75	0.31	0.29	0.65	0.86	0.76	0.83	0.92	0.94	0.95	0.35	0.05
2.00	0.35	0.34	0.69	0.87	0.81	0.87	0.95	0.96	0.97	0.14	0.02
3.00	−0.05	0.01	0.32	0.56	0.43	0.47	0.59	0.63	0.74	0.72	0.005

TABLE XII. Same as in Table VII, but for W with cross section units of 10^{-40} cm^2/(GeV/c^2) and covariance units of 10^{-80} cm^4/(GeV/c^2)^2.

	1.00	1.10	1.20	1.30	1.40	1.50	1.60	1.70	1.80	2.00	2.25	2.50
$\frac{d\sigma}{dW}$	6.11	20.4	35.2	39.2	43.5	48.2	46.8	37.8	25.1	10.7	3.81	0.95
GENIE	5.26	18.3	33.0	34.4	37.4	43.1	43.8	35.0	21.9	8.94	3.04	0.68
1.00	3.88	9.39	6.68	5.53	6.06	7.06	9.86	7.59	2.98	1.41	−0.35	−0.49
1.10	0.93	26.3	19.5	13.3	14.5	17.7	27.1	21.9	9.92	5.05	−0.06	−0.72
1.20	0.73	0.82	21.6	16.8	15.1	16.6	21.5	15.8	8.24	5.49	1.07	−0.01
1.30	0.63	0.58	0.81	20.0	20.0	21.2	19.5	13.7	6.21	2.46	−0.43	−0.88
1.40	0.60	0.55	0.63	0.87	26.4	29.3	25.8	19.5	8.05	0.90	−1.96	−1.85
1.50	0.60	0.58	0.59	0.79	0.95	36.2	32.3	24.4	9.91	1.40	−2.36	−2.34
1.60	0.81	0.86	0.75	0.71	0.81	0.87	37.9	30.3	13.7	4.18	−1.14	−1.62
1.70	0.75	0.83	0.66	0.59	0.74	0.79	0.95	26.6	12.5	3.32	−0.72	−1.08
1.80	0.55	0.71	0.65	0.51	0.57	0.60	0.81	0.89	7.52	2.29	0.62	0.11
2.00	0.41	0.56	0.68	0.32	0.10	0.13	0.39	0.37	0.48	3.04	1.26	0.54
2.25	−0.17	−0.01	0.21	−0.09	−0.35	−0.36	−0.17	−0.13	0.21	0.67	1.16	0.68
2.50	−0.36	−0.20	−0.00	−0.29	−0.52	−0.57	−0.38	−0.30	0.06	0.45	0.91	0.47

[1] M. A. Acero *et al.* (NOvA Collaboration), Phys. Rev. D **98**, 032012 (2018).

[2] B. Abi *et al.* (DUNE Collaboration), arXiv:2002.03005.

[3] G. M. Radecky *et al.* (ANL Collaboration), Phys. Rev. D **25**, 1161 (1982).

[4] T. Kitagaki *et al.* (BNL Collaboration), Phys. Rev. D **34**, 2554 (1986).

[5] T. Le *et al.* (MINERvA Collaboration), Phys. Lett. B **749**, 130 (2015).

[6] O. Altinok *et al.* (MINERvA Collaboration), Phys. Rev. D **96**, 072003 (2017).

[7] D. Coplowe *et al.* (MINERvA Collaboration), Phys. Rev. D **102**, 072007 (2020).

[8] A. A. Aguilar-Arevalo *et al.* (MiniBooNE Collaboration), Phys. Rev. D **83**, 052009 (2011).

[9] C. Mariani (K2K Collaboration), AIP Conf. Proc. **967**, 174 (2007).

[10] C. Adams *et al.* (MicroBooNE Collaboration), Phys. Rev. D **99**, 091102 (2019).

[11] P. Adamson *et al.*, Nucl. Instrum. Methods Phys. Res., Sect. A **806**, 279 (2016).

[12] S. Mufson *et al.*, Nucl. Instrum. Methods Phys. Res., Sect. A **799**, 1 (2015).

[13] T. T. Böhlen, F. Cerutti, M. P. W. Chin, A. Fassò, A. Ferrari, P. G. Ortega, A. Mairani, P. R. Sala, G. Smirnov, and V. Vlachoudis, Nucl. Data Sheets **120**, 211 (2014).

[14] A. Ferrari *et al.*, CERN Technical Report No. CERN-2005-010, SLAC-R-773, INFN-TC-05-11, 2005.

[15] M. Campanella *et al.*, CERN Technical Report No. ATL-SOFT-99-004, ATL-COM-SOFT-99-004, CERN-ATL-SOFT-99-004, 1999.

[16] L. Aliaga *et al.* (MINERvA Collaboration), Phys. Rev. D **94**, 092005 (2016); **95**, 039903(A) (2017).

[17] C. Andreopoulos *et al.* (GENIE Collaboration), Nucl. Instrum. Methods Phys. Res., Sect. A **614**, 87 (2010).

[18] S. Dytman, AIP Conf. Proc. **896**, 178 (2007).

[19] S. Dytman, Acta Phys. Pol. B **40**, 2445 (2009).

[20] C. H. Llewellyn Smith, Phys. Rep. **3**, 261 (1972).

[21] D. Rein and L. M. Sehgal, Ann. Phys. (N.Y.) **133**, 79 (1981).

[22] A. Bodek and U. K. Yang, J. Phys. G **29**, 1899 (2003).

[23] T. Katori, AIP Conf. Proc. **1663**, 030001 (2015).

[24] S. Agostinelli *et al.* (GEANT4 Collaboration), Nucl. Instrum. Methods Phys. Res., Sect. A **506**, 250 (2003).

[25] C. N. Chou, Phys. Rev. **87**, 904 (1952).

[26] A. Aurisano, C. Backhouse, R. Hatcher, N. Mayer, J. Musser, R. Patterson, R. Schroeter, and A. Sousa (NOvA Collaboration), J. Phys. Conf. Ser. **664**, 072002 (2015).

[27] R. Workman *et al.* (Particle Data Group), Prog. Theor. Exp. Phys. **2022**, 083C01 (2022).

[28] M. Ester *et al.*, in *Proceedings of the 2nd International Conference on Knowledge Discovery and Data Mining* (Association for the Advancement of Artificial Intelligence (AAAI), Washington, DC, 1996), pp. 226–231.

[29] M. Baird, J. Bian, M. Messier, E. Niner, D. Rocco, and K. Sachdev, J. Phys. Conf. Ser. **664**, 072035 (2015).

[30] J. C. Dunn, J. Cyber. **3**, 32 (1973).

[31] R. E. Kalman, J. Basic Eng. **82**, 35 (1960).

[32] N. J. Raddatz, Ph.D. thesis, University of Minnesota (2016), FERMILAB-THESIS-2016-05.

[33] D. S. Pershey, Ph.D. thesis, Caltech (2018), FERMILAB-THESIS-2018-17.

[34] All quoted resolutions are calculated as the rms difference between reconstructed and true values in simulation.

[35] A. Aurisano, A. Radovic, D. Rocco, A. Himmel, M. D. Messier, E. Niner, G. Pawloski, F. Psihas, A. Sousa, and P. Vahle, J. Instrum. **11**, P09001 (2016).

[36] G. D'Agostini, Nucl. Instrum. Methods Phys. Res., Sect. A **362**, 487 (1995).

[37] G. D'Agostini, arXiv:1010.0632.

[38] C. Andreopoulos *et al.* (GENIE Collaboration), arXiv:1510.05494.

[39] J. M. Conrad, M. H. Shaevitz, and T. Bolton, Rev. Mod. Phys. **70**, 1341 (1998).

[40] E. S. Pinzon Guerra *et al.* (DUET Collaboration), Phys. Rev. C **95**, 045203 (2017).

[41] D. Ashery, I. Navon, G. Azuelos, H. K. Walter, H. J. Pfeiffer, and F. W. Schlepütz, Phys. Rev. C **23**, 2173 (1981).

[42] J. B. Birks, Proc. Phys. Soc. London Sect. A **64**, 874 (1951).

[43] M. Agostini *et al.* (Borexino Collaboration), Astropart. Phys. **97**, 136 (2018).

[44] P. Adamson *et al.* (NOvA Collaboration), Phys. Rev. Lett. **118**, 151802 (2017).

[45] J. A. Formaggio and G. P. Zeller, Rev. Mod. Phys. **84**, 1307 (2012).

[46] M. Kabirnezhad, Phys. Rev. D **97**, 013002 (2018).